Journal of Molecular Catalysis A: Chemical 320 (2010) 47–55

Contents lists available at ScienceDirect

Journal of Molecular Catalysis A: Chemical

journal homepage: www.elsevier.com/locate/molcata

Partial oxidation of methane over bimetallic copper–cerium oxide catalysts

Ana C. Ferreira[a], A.M. Ferraria[b], A.M. Botelho do Rego[b], António P. Gonçalves[a], A. Violeta Girão[c], Rosário Correia[d], T. Almeida Gasche[a], Joaquim B. Branco[a,*]

[a] Instituto Tecnológico e Nuclear, Unidade de Ciências Químicas e Radiofarmacêuticas, Estrada Nacional 10, 2686-953 Sacavém, Portugal
[b] Universidade Técnica de Lisboa, IST, Centro de Química - Física Molecular and IN, Av. Rovisco Pais, 1049-001 Lisboa, Portugal
[c] Universidade de Aveiro, CICECO, Campus Universitário de Santiago, 3810-193 Aveiro, Portugal
[d] Universidade de Aveiro, I3N- Departamento de Física, Campus Universitário de Santiago, 3810-193 Aveiro, Portugal

ARTICLE INFO

Article history:
Received 30 May 2009
Received in revised form
14 December 2009
Accepted 24 December 2009
Available online 11 January 2010

Keywords:
Bimetallic
Copper–cerium oxide
Methane
Catalytic partial oxidation

ABSTRACT

The performance of bimetallic copper–cerium oxides was investigated for the catalytic partial oxidation of methane. They were synthesized by two routes using either the intermetallic compound $CeCu_2$ as catalytic precursor or the sol–gel method via cerium and copper nitrates (1:2) in the presence of urea. The catalysts prepared by the sol–gel method were always less active and selective than the catalyst prepared by the intermetallic route, which was comparable in catalytic behavior to noble metal catalysts on alumina (e.g. 5 wt% Rh/Al_2O_3, Conv. $CH_4 > 90\%$, Sel. $H_2 > 99\%$, $H_2/CO \approx 2.0$) at $T = 750\,^{\circ}C$. To our knowledge, this is a novelty for copper based catalysts. The copper–cerium oxide catalysts were also quite stable in the temperature range studied, 350–800 °C, and for a long period of time on stream. Such catalytic behavior seems to be determined by the surface morphology and composition and by an unusual interaction between the copper and cerium oxide that hinders the deactivation of the catalyst at high temperatures, which is a direct consequence of the synthetic method used in this work. Therefore, the bimetallic copper–cerium oxide catalyst obtained by the intermetallic route seem to be a good option to produce syngas with the advantage of being less expensive than the catalysts based on noble metals.

1. Introduction

The development of efficient catalysts for the oxidation of methane and other volatile organic compounds (VOC's) has attracted renewed attention during the last years. For the industry, methane is a source of hydrogen (fuel cell technology) and an important precursor of syngas that can be used for the production of hydrocarbons (via Fischer–Tropsch synthesis). For the environment, methane is a pollutant.

The catalytic partial oxidation of methane (POM) constitutes a proper way to produce syngas [1]. This reaction is mildly exothermic and provides a suitable H_2/CO ratio for the methanol and Fischer–Tropsch synthesis. These characteristics make POM an attractive and realistic alternative to the steam reforming reaction.

The catalysts reported to be active for the POM to syngas are either noble metals (like Ir, Pt, Pd, Rh and particularly Ru) or Ni-based compounds [2–6]. Despite the high activity of noble metal based catalysts, the high cost of such systems limits their extensive industrial application. Ni catalysts, usually supported on alumina or silica, have been also extensively studied [7–10]. However, the major drawbacks of this reaction are the deactivation caused by sintering, changes in the oxidation state of the metal active phase and carbon deposition [1]. The most obvious way to minimize these phenomena is to work at lower temperatures; however the methane partial oxidation reaction has to proceed at high temperatures (usually higher than 700 °C) to achieve significant conversion of methane [11].

Many efforts have focused on the development of metal catalysts with long-term operation stability. Noble metal catalysts are less sensitive to carbon deposition than other catalysts [12–14]. However, the use of nickel perovskite-type oxides seems also a good alternative to reduce the formation and deposition of carbon on the catalysts. Lago et al. [15] observed that the activity and selectivity of a series of $LnCoO_3$ (Ln = La, Pr, Nd, Sm, or Gd) perovskites was high for the POM reaction to syngas. Choudhary et al. [16] reported that complex oxides with a perovskite structure, like $LaNiO_3$, $La_{0.8}Ca$ (or Sr)$_{0.2}NiO_3$ and $LaNi_{1-X}Co_XO_3$ ($X = 0.2–1.0$), were resistant to coking. Tsipouriari and Verykios [17] studied the partial oxidation of methane to synthesis gas over a Ni/La_2O_3 catalyst and have found that the CH_4 conversion and the H_2 selectivity were close to thermodynamic predictions.

On the other hand, the ability of ceria to store, release and transport oxygen makes it very attractive as catalyst in oxidation reactions. Cerium is capable of adjusting its electronic configura-

* Corresponding author. Tel.: +351 219946116.
E-mail address: jbranco@itn.pt (J.B. Branco).

1381-1169/$ – see front matter © 2010 Elsevier B.V. All rights reserved.
doi:10.1016/j.molcata.2009.12.014

tion [18] and ceria itself has catalytic activity for the oxidation of methane [19,20]. Otsuka et al. [21–23] showed that ceria is able to directly convert methane to syngas at temperatures higher than 600 °C.

Ceria was also used as a promoter of both the activity and selectivity of supported Ni or Pt catalysts for partial oxidation of methane [24,25] or CO_2 reforming of methane [26]. Tang et al. [27] reported that nickel supported on ceria (high Ni-loading of 13 wt%) was active for POM at T = 750 °C. However, this catalyst rapidly deactivates due to carbon deposition.

In recent years, Cu–Ce–O composite catalysts received considerable attention [28–31]. Their high catalytic activity seems to be connected to both CuO and CeO_2 [28,29]. In 1995, Liu reported that CuO–CeO_2 catalysts were very active for the oxidation of methane in the presence of CO, conversion ≈95% [32]. Other copper–ceria-based materials have been regularly examined as active catalysts for total oxidation reactions, such as CO oxidation [29,32–34] and CH_4 combustion [29,32,35,36].

The influence of the preparation method was also reported by various researchers. Several methods for the preparation of copper–cerium oxide catalysts were used such as combustion, thermal decomposition, co-precipitation and sol–gel [28,31,37]. Compared with other methods, sol–gel has advantages such as (i) easy control of the chemical composition and (ii) low-temperature synthesis and has been employed to prepare different types of materials [38].

In this context, binary intermetallic compounds of lanthanide or actinide metals combined with *d* metals (namely Ni, Co, Mn, or Fe) have drawn the attention of many authors due to their catalytic properties [39–47] and were described as a new type of supported catalysts precursors, which can be more active and selective than those obtained by conventional routes [40–42,45–51].

In our laboratories, we have been using binary intermetallic compounds $LnCu_2$ (Ln = La, Ce, Pr, Nd) [40], $ThCu_2$ and $AnNi_2$ (An = Th, U) as catalytic precursors of bimetallic oxides, e.g. $3CuO{\cdot}Ln_2CuO_4$ or $2CuO{\cdot}ThO_2$ [42]. Such compounds exhibited selectivity for the 4-methylpentan-2-ol decomposition and the lanthanide-containing phase, CeO_2 or Ln_2CuO_4, seems to play a role in the formation of the CuO active sites [40]. After reduction, these bimetallic oxides were described as supported copper catalysts on lanthanide oxides, $2Cu{\cdot}CeO_2$ and $4Cu{\cdot}Ln_2O_3$, which were active and selective for the mesityl oxide hydrogenation to 4-methylpentan-2-one (methylisobutylketone, MIBK) [51]. Their catalytic activity and selectivity was associated with the lanthanide-containing phase that seems to play an important role in the formation of the copper and/or nickel active sites.

Here we report and compare the activity, selectivity and stability of bimetallic copper–cerium oxide catalysts for catalytic gas-phase partial oxidation of methane in the temperature range of 350–850 °C and at atmospheric pressure. They were prepared by two routes using either the intermetallic $CeCu_2$ as catalytic precursor or the sol–gel method. All the samples were characterized by powder X-ray diffraction (XRD), scanning electron microscopy (SEM), energy dispersive X-ray spectrometry (EDS), UV-Raman spectrometry (RAMAN), X-ray photoelectron spectroscopy (XPS) and temperature-programmed reduction (H_2-TPR).

2. Experimental

2.1. Catalysts preparation

The bimetallic copper–cerium oxides were prepared by two routes: (i) the intermetallic route (sample $2CuO{\cdot}CeO_2$) using the controlled oxidation of $CeCu_2$ under air (Air Liquide, O_2:N_2 = 20:80 (vol.%), purity 99.995%) at 10 °C/min heating rate up to 950 °C, as described elsewhere [40] and (ii) the sol–gel route (samples $CeCu_2O_4$) using the reaction of aqueous solutions containing stoichiometric amounts of Ce(III) and Cu(II) nitrates (Aldrich, purity 99.99% cerium nitrate; purity 98.0% copper nitrate) in the presence of urea (Panreac, purity 99.0%). All the reagents were used without further purification. The initial concentrations were 0.1 M in Ce(III), 0.2 M in Cu(II), and 3 M in urea. The volume of the initial solution (blue color) was 100 mL. The water of this solution was evaporated on a hot-plate at 80 °C with continuous stirring and a gel formed upon cooling. This gel was decomposed in an oven at 250 °C to yield the precursor, sample $CeCu_2O_4$250, and calcined at two different temperatures, 600 and 900 °C in order to obtain samples with different mean particle size (samples $CeCu_2O_4$ 600 and $CeCu_2O_4$ 900, respectively). Calcination time was 7 h for all three samples [52].

2.2. Catalyst characterization

XRD patterns were obtained in reflection geometry with a PANalitycal X'Pert Pro diffractometer using Cu Kα monochromatic radiation (λ = 1.5406 Å). The operational settings for all scans were voltage = 45 kV; current = 40 mA; 2θ scan range 5–80° using a step size of 0.03° at a scan speed of 0.02°/min. For identification purposes, the relative intensities (I/I_0) and the *d*-spacing (Å) were compared with standard JCPDS powder diffraction files [53]. The mean CuO and CeO_2 particle diameter were determined by means of the Scherrer's equation using the XRD (0 0 2) and (1 1 1) peaks, respectively [54].

The surface morphology and the particle size of the samples were obtained using a HR-FESEM Hitachi SU-70, operating at 15 keV. The chemical composition was determined by EDS, using a B-U Bruker Quantax 400 EDS system (EDS data available as supplementary material).

The X-ray photoelectron spectroscopy (XPS) measurements were performed in a spectrometer XSAM800 (KRATOS) operated in the fixed analyzer transmission (FAT) mode, with pass energy of 20 eV. The non-monochromatized Al Kα X-radiation of 1486.6 eV was produced using a current of 10 mA and a voltage of 12 kV. Samples were analyzed at 45° takeoff angle (TOA) in an ultrahigh vacuum (UHV) chamber (<10^{-7} Pa) at room temperature. Details on spectra acquisition and data treatment were published elsewhere [55]. For quantification purposes, sensitivity factors were 0.66 for O 1s, 0.25 for C 1s, 6.3 for Cu 2p and 10.0 for Ce 3d.

Raman spectra (Stokes) were taken in the backscattering configuration at room temperature and analyzed using a LabRaman HR800/UV (Jobin-Yvon) spectrometer. The samples were excited with a He–Cd laser (325 nm) and the microscope attachment is based on an NUV system that uses a 40× long distance objective.

H_2-TPR experiments were performed under pure hydrogen in an apparatus previously described [42,51]. The samples were placed in a quartz U tube (6 mm diameter), then submitted to a flow of hydrogen (50 cm^3/min) under atmospheric pressure, and heated up to 950 °C at a rate of 10 °C/min. The degree of reduction was determined by the quantitative analysis of water, the reduction product, as described elsewhere [56]. This procedure allows enhancing the sensitivity of the method as well as performing TPR experiments under pure hydrogen. Prior to H_2-TPR, all samples were pretreated at 150 °C under He (F = 50 cm^3/min) during 10 min to eliminate any problem due to physisorbed water. Optimized resolution was obtained by careful choice of the sample weight (≤30 mg) and hydrogen flow (F = 50 cm^3/min) taking into account the criteria established by Ballivet-Tkatchenko and Delahay [57] for the temperature-programmed reduction of V_2O_5 that we have also confirmed for the reduction of CuO. The TPR curves became distorted, flat at their maximum and there is a broadening of the peaks for K > 20 s (P > 3 °C) and the optimal conditions comprise between

10–20 s and 1.5–3 °C for K and P, respectively. Under our experimental conditions, the calculated K and P values were ≈15 s and ≈3 °C. Water was analyzed on a Shimadzu 9A instrument equipped with thermal conductivity detector (TCD), helium was used as carrier gas (F = 50 cm^3/min, $T_{Detector}$ = 105 °C, 150 mA), connected to a CR3 Shimadzu integrator.

2.3. Catalytic activity

The catalytic partial oxidation of methane was carried out at atmospheric pressure in a fixed-bed U-shaped quartz reactor, plug-flow type reactor, with a quartz frit and an inside volume of 15 cm^3. Mass flow controllers were used to control CH_4 (Air Liquide, purity 99.9995%), air (Air Liquide, purity 99.9995%) and He (Air Liquide, purity 99.9995%) flows. A thermocouple was placed near the catalytic bed for continuous monitoring of the sample temperature. Unless otherwise stated, a gaseous mixture with a CH_4/O_2 molar ratio of 2 [CH_4 (28%), air (O_2 14%, N_2 58%)] was used and the reaction studied with an adequate Gas Hourly Space Velocity (GHSV, mL of CH_4/g catalyst h) of 8500, m = 100 mg. The outlet gas was cooled in an ice-water trap and their composition analyzed on-line by gas chromatography using a Restek ShinCarbon ST column (L = 2.0 m, ϕ = 1/8 in., ID = 1 mm, 100/200 mesh) and an Agilent 4890D GC equipped with a thermal conductivity detector (TCD) and a 6-port gas sampling valve with a 0.250 μL loop.

Catalyst activity (r_i) was defined as the number of mL of methane converted per g of catalyst and per hour (mL_{CH_4}/g h). Unless otherwise stated, the values reported in this paper represent the activities of the catalysts after 1 h on stream. The conversion of CH_4, the selectivities of CO, CO_2, C2 ($C_2H_4 + C_2H_6$) and H_2 were calculated as follows: $Conv._{CH_4}$ (%) = $\{([CH_4]_i - [CH_4]_o)/[CH_4]_i\} \times 100$; $Sel._{CO}$ (%) = $\{[CO]_o/([CH_4]_i - [CH_4]_o)\} \times 100$; $Sel._{CO_2}$ (%) = $\{[CO_2]_o/([CH_4]_i - [CH_4]_o)\} \times 100$; $Sel._{C2}$ (%) = $\{2 \times [C2]_o/([CH_4]_i - [CH_4]_o)\} \times 100$ and $Sel._{H_2}$ (%) = $\{[H_2]_o/2 \times ([CH_4]_i - [CH_4]_o)\} \times 100$, where $[CH_4]_i$ is the inlet flow rate of methane and $[CH_4]_o$, $[CO]_o$, $[CO_2]_o$, $[C2]_o$ and $[H_2]_o$ are outlet flow rates for methane and products. The amount of reagents and products was confirmed by an external standard method using reference mixtures of CH_4, CO, CO_2, H_2 and C_2 (Air Liquide). The confidence level was better than 95%. The activity of the catalysts was compared to that of a commercial catalyst (5.0 wt% Rh/Al_2O_3, Aldrich), one standard in this research field [58].

3. Results and discussion

3.1. Catalysts characterization

Fig. 1 shows the X-ray diffraction patterns obtained before catalytic tests. For both series of copper–cerium oxides, sol–gel and intermetallic samples, the patterns were consistent with those of standard CuO and CeO_2 monoclinic and cubic phases, respectively, reported before for the oxidation of $CeCu_2$ [40], with a nearly absence of differences in the respective lattice parameters.

However, the surface morphology of the copper–cerium oxides particles was significantly different depending on the synthetic method. The analysis by SEM/EDS shows that the copper–cerium oxide obtained by the intermetallic route is composed by aggregates of CeO_2 with variable size and platelets of CuO, whereas the sol–gel samples appear to be better described as a homogeneous solution of both oxides (EDS data available as supplementary material) (Fig. 2). The average particle size is ≈50 nm in the case of the sol–gel samples, which agrees well with the values calculated from the Scherrer's equation (40–60 nm).

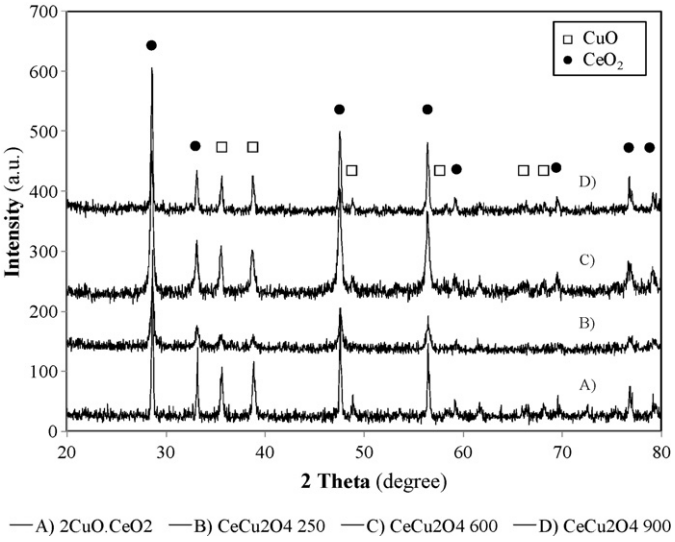

Fig. 1. XRD patterns for the bimetallic copper–cerium oxides obtained by the intermetallic route (A) and by sol–gel (urea) after calcination at 250 °C (B); 600 °C (C) and 900 °C (D).

To further characterize the sol–gel and the intermetallic samples, temperature-programmed reduction (H_2-TPR) and Raman studies were also undertaken. Fig. 3 shows the Raman spectra obtained for all the copper–cerium oxides that are dominated by two main peaks at 466 and 1175 cm^{-1}, which were assigned to cubic CeO_2 [59,60]. Two minor bands were also observed at about 298 and 623 cm^{-1}.

The frequency at 466 cm^{-1} is related to symmetrical stretching of the Ce–O_8 vibrational unit, corresponding to the triply degenerate F_{2g} mode of fluorite CeO_2 and the only one allowed in first order Raman scattering. The bands at about 623 and 1175 cm^{-1} were linked to activation of density of states of phonon (DOS) in CeO_2 lattice due to the presence of CeO_2 defects that induce the relaxation of Raman selection rules. These bands are related, respectively, to Raman inactive transverse and longitudinal optical phonon modes at the Brillouin zone center and were linked to oxygen vacancies in the CeO_2 lattice [60–62]. Since oxygen vacancies are active sites for combustion reactions, this finding confirms that copper–lanthanide oxides are promising for applications in catalytic oxidation processes. The almost undetectable band at 298 cm^{-1} was assigned to CuO, which could indicate that copper species are well dispersed and in close contact with CeO_2 [63]. However, the nearly absence of differences in the respective lattice parameters of the CeO_2 fluorite type cell suggests that no large amount of copper has been incorporated in the lattice [60,64,65].

Fig. 4 shows typical H_2-TPR profiles obtained for the reduction of $2CuO{\cdot}CeO_2$ (intermetallic route) and $CeCu_2O_4$ catalysts obtained by the sol–gel/urea route after calcination at 250, 600 and 900 °C.

The H_2-TPR profiles show one main reduction peak in the temperature range of 174–265 °C and a second reduction peak between 687 and 701 °C (see inset). For the first reduction peak, the temperature at maximum mass loss rate (Tm) increases with the calcination temperature, except for the sample calcined at 250 °C. For the second mass losses the Tm is practically independent of the calcination temperature, within the experimental error (±5 °C).

The standard Gibbs free energy for copper oxide reduction is considerably more favorable than that of CeO_2 into Ce_2O_3 (e.g. −98.9 kJ/mol for the reduction of CuO and +24.4 kJ/mol for the reduction of CeO_2) [66]. Therefore, the reduction of CuO is expected at first and the Tm of the first reduction peaks was attributed to the reduction of CuO [40,42,51]. The Tm of second reduction peaks fits the published data for the surface reduction of CeO_2 [67]. The XRD

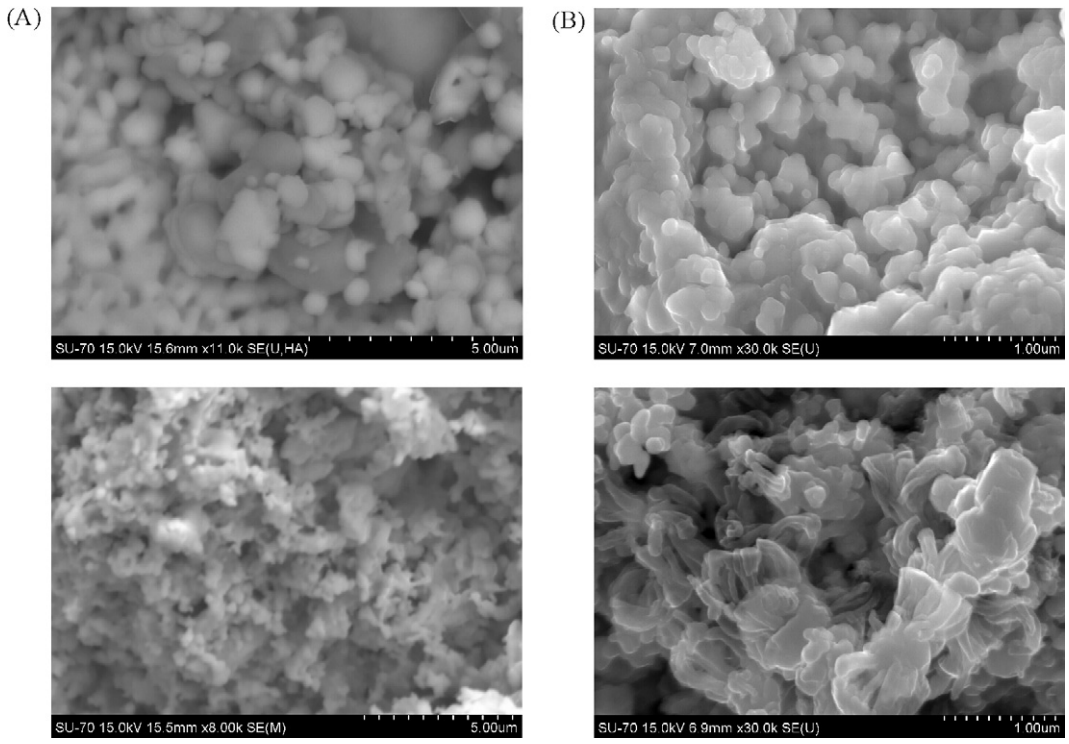

Fig. 2. SEM images obtained before (upper) and after reaction (lower) for the bimetallic copper–cerium oxides: (A) intermetallic route, (B) sol–gel reaction, calcination at 900 °C.

patterns obtained after the H_2-TPR study were identical to those already published for the reduction of $2CuO{\cdot}CeO_2$ that show pure crystalline phase of metallic copper along with CeO_2 [68], which confirms that the second reduction peaks correspond to the surface reduction of CeO_2 instead of a bulk reduction with formation of Ce_2O_3 [67,68].

The H_2-TPR quantitative analysis of the water produced on each mass loss gives a H_2O:Ce molar ratio of 2.2, 1.9, 2.2 and 2.1 ± 0.2 for $2CuO{\cdot}CeO_2$ (intermetallic route), $CeCu_2O_4$ 900, $CeCu_2O_4$ 600 and $CeCu_2O_4$ 250 (sol–gel route), respectively. The *T*m obtained for the first reduction peak of the sol–gel samples is lower than that of pure CuO, whereas in the case of $2CuO{\cdot}CeO_2$ it shifts to higher temperature. Moreover, the *T*m is lower for the samples calcined at 600 and 900 °C than for that calcined at 250 °C (222 *vs.* 174 or 192) that present a temperature at maximum reduction rate corresponding to that of pure CuO, within the *T*m experimental error (±5 °C). One possible answer to such difference can be found on the amorphous character of the sample calcined at 250 °C, compared to the XRD behavior of the other samples (Fig. 1), which could indicate that the sample calcined at 250 °C behave as a mixture of highly dispersed nanoparticles of pure oxides (CuO plus CeO_2) without any contact between them.

Liu and Flytzani-Stephanopoulos [33] reported *T*m values for the reduction of copper oxide clusters strongly interacting with ceria in the temperature range of 125–175 °C, while larger CuO particles, non-associated with CeO_2, were reduced at ≈200 °C. Wrobel et al. [69] reported copper reduction in the range of 120–150 °C for CuO/CeO_2 catalysts. The same results were also reported by Ratnasamy et al. [70], where two overlapping reductions were attributed to disperse copper oxide clusters, strongly interacting with CeO_2.

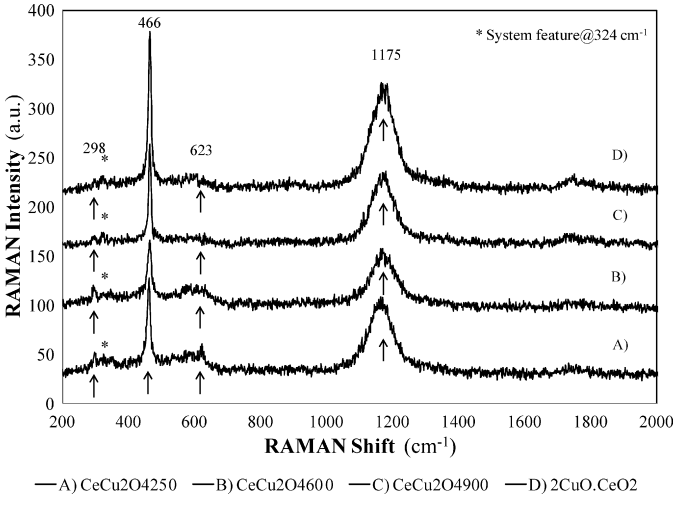

Fig. 3. UV-RAMAN spectra for the bimetallic copper–cerium oxide obtained by the sol–gel and the intermetallic routes.

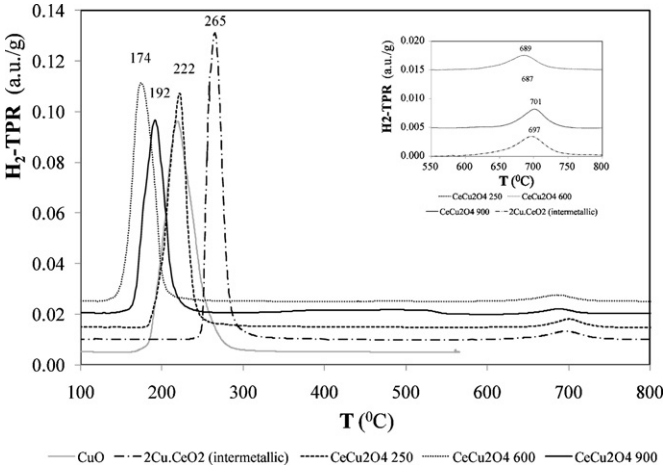

Fig. 4. H_2-TPR profiles for the bimetallic copper–cerium oxides and pure CuO.

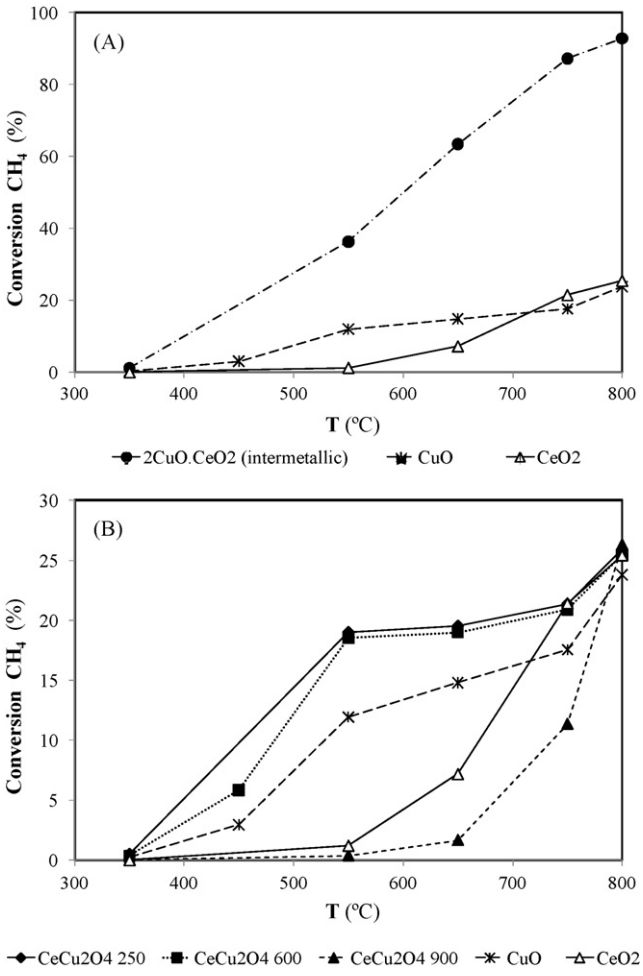

Fig. 5. Temperature effect on the conversion of methane over the bimetallic copper–cerium oxides: (A) intermetallic and (B) sol–gel route.

Therefore, the H_2-TPR results of the copper–lanthanide oxides obtained by the sol–gel route may be attributed to reduction and formation of highly dispersed CuO that strongly interacts with CeO_2 thus lowering the temperature at the maximum mass loss rate (except for the sample calcined at 250 °C) [71]. To explain the result obtained with the intermetallic sample, the possibility of an unusual synergistic effect between CuO and CeO_2 that lead to a higher reduction temperature must be taken into account, which is certainly connected to this unusual synthetic route that provide bimetallic copper–cerium oxides more stable to reduction.

3.2. Activity and stability of catalysts

The copper–cerium oxides were active and selective for the catalytic partial oxidation of methane. The conversion of methane becomes measurable in the temperature range of 350–800 °C and increases with the reaction temperature (Fig. 5).

The catalyst obtained by the intermetallic route presents always the highest activity and converts about 90% of methane at 750 °C (Fig. 5A), whereas over the sol–gel samples the conversion of methane is considerably lower ≈20% (Fig. 5B). Among the copper–cerium oxides obtained by the sol–gel method, the catalysts calcined at 250 and 600 °C presented the same performance: become active at 350 °C and reach an activity of about 20% at $T \geq 550$ °C. The catalyst calcined at 900 °C was inactive until $T = 650$ °C but at 800 °C, the conversion of methane was ≈20%, as for the other sol–gel samples. For comparison proposes, the study of

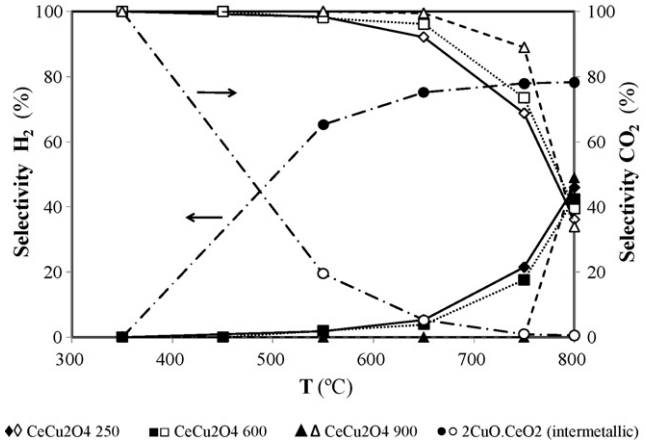

Fig. 6. Temperature effect on the selectivity to hydrogen (bold symbols) and carbon dioxide (open symbols) over the bimetallic copper–cerium oxides.

POM over CuO and CeO_2 was also undertaken. Pure CeO_2 was inactive at $T \leq 650$ °C, whereas the activity of pure CuO starts at 450 °C. Higher temperatures increase dramatically the activity of CeO_2 that at $T \geq 750$ °C becomes equal to that of pure CuO ≈ 20% and to that of the copper–cerium oxides obtained by the sol–gel route.

Through the analysis of the catalytic performance for all the samples, it can be said that the synthetic method used for preparation of the catalysts influence the activity and thus the calcination temperature of the sol–gel samples, however in terms of a small effect. As shown in Fig. 6, the selectivity to hydrogen is always lower over the $CeCu_2O_4$ catalysts (sol–gel samples) than over $2CuO{\cdot}CeO_2$ (intermetallic sample). In contrast, carbon dioxide was the main product over the sol–gel catalysts ($T < 650$ °C), whereas the selectivity to CO_2 decreased significantly with the temperature over $2CuO{\cdot}CeO_2$ and became residual (<2%) at $T \geq 650$ °C.

Moreover, the activity of $2CuO{\cdot}CeO_2$ is only comparable to that of catalysts based on noble metals ($T \geq 550$ °C) reported to be very active for the POM to syngas reaction [2–6]. As an example, it was found that the behavior of $2CuO{\cdot}CeO_2$ at 800 °C is similar to that of a commercial catalyst of rhodium (5 wt%) on alumina (Table 1). Therefore, it seems to be a good alternative to produce syngas since it provides at $T \geq 550$ °C a suitable H_2/CO ratio of ≈2 for the methanol and Fischer–Tropsch synthesis, with the advantage of being less expensive than the noble metal catalysts.

The bimetallic copper–cerium oxides activity and selectivity was also quite stable in the temperature range studied (350–800 °C) and for a long period of time on stream. Fig. 7 shows the performance of the sol–gel, intermetallic and rhodium samples at 800 °C. For all the samples and at each temperature studied (350, 450, 550, 650, 750 and 800 °C), no deactivation was observed for a period of ≈18 h of time on stream (total time on stream superior to 100 h).

To our knowledge, the results obtained over $2CuO{\cdot}CeO_2$ are a novelty on copper based catalysts, which corroborate the advantage of the intermetallic compound $CeCu_2$ as precursor for the preparation of bimetallic copper–cerium oxide catalysts.

Table 1
Ce/Cu, O/(Ce + Cu) and C/(Ce + Cu) atomic ratios computed from the XPS Ce 3d, Cu 2p, O 1s and C 1s core level peaks, before and after reaction.

Catalysts	Ce/Cu	O/(Ce + Cu)	C/(Ce + Cu)
$2CuO{\cdot}CeO_2$	0.6 (0.3)[a]	2.6 (2.1)	1.9 (1.0)
$CeCu_2O_4$ 250	0.6 (0.9)	1.9 (2.2)	1.2 (2.7)
$CeCu_2O_4$ 600	0.7 (0.8)	1.7 (1.9)	1.1 (1.9)
$CeCu_2O_4$ 900	0.7 (0.5)	2.3 (1.9)	1.0 (3.8)

[a] Within parentheses the values obtained after reaction.

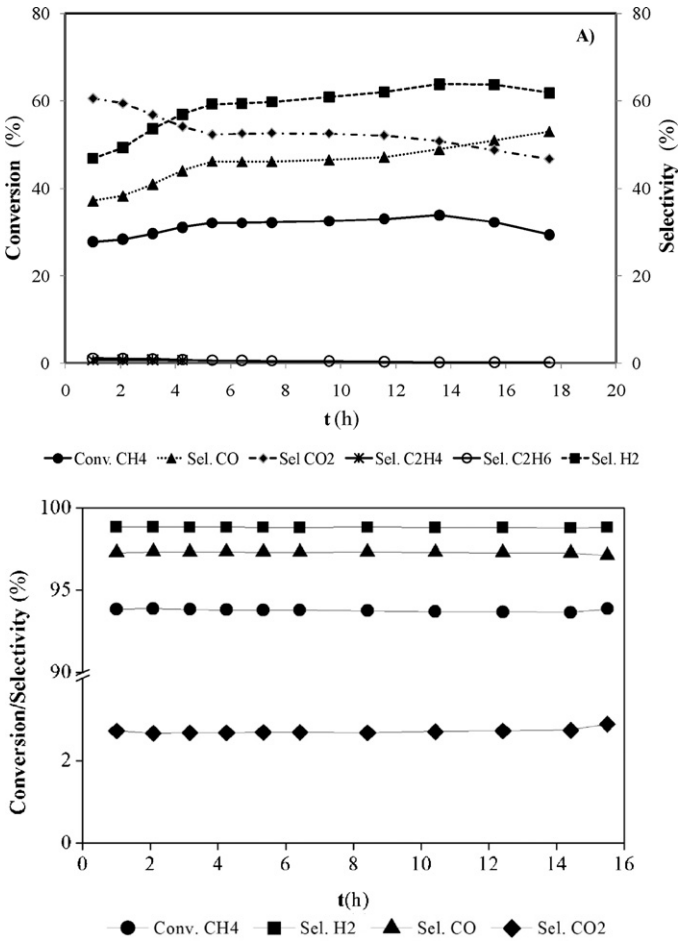

Fig. 7. Partial oxidation of methane over the bimetallic copper–cerium oxide as a function of time on stream at 800 °C: (A) samples obtained by the sol–gel reaction and by (B) sample obtained by the intermetallic route and commercial catalyst 5 wt% Rh/Al_2O_3.

This raises the question about the nature of the active sites for the catalytic POM over copper–lanthanide oxides and the roles played by copper and ceria on their formation. Ceria is catalytically active for the oxidation of methane [19,20]. Otsuka et al. [21–23] showed that ceria is able to directly convert methane to syngas at temperatures higher than 600 °C. Moreover, recent studies have shown that the oxygen vacancies in ceria are very efficient for the activation of gold and copper nanoparticles for the water gas shift reaction [72–74].

In order to explain our results and to approach the true nature of the active sites, an analysis of the catalysts after reaction was undertaken. Figs. 2 and 8 show some of the SEM pictures obtained after reaction (AR). Important modifications occur on the bimetallic copper–cerium oxides surface morphology that in the case of the intermetallic catalyst become more porous, whereas in the case of the sol–gel samples the surface is now composed of aggregates of cerium oxide grains and platelets of copper oxide (EDS analysis shows evidence of copper agglomerations at the surface) (Fig. 2). Sample $CeCu_2O_4$250 shows also evidence of few tubes that morphologically appear to be carbon nanotubes (Fig. 8A), which was confirmed by the analysis of the sample after a long period of time on stream (Fig. 8B). The surface of the sample is covered by tubular structures that appear to be carbon nanotubes with variable diameter (≈30–70 and 100 nm) and variable length.

However, the element mapping shows that cerium is clearly detected in the place of tubes (EDS, supplementary material). Nevertheless, quantification of carbon by SEM-EDX is not possible in these conditions because the powders were previously covered with a thin film of carbon of which the thickness cannot be measured without adequate equipment in order to obtained proper secondary images from SEM. The average particle size was comparable to those obtained before reaction.

After reaction and especially after a long period of time on stream (stability studies), the formation of other oxide phases that could correspond to the formation of new solid solutions between CuO and CeO_2 was by no means detected. However, the appearance of Cu_2O (Fig. 9) and Cu (Fig. 10) due to copper oxide partial and total reduction, respectively, was identified by XRD.

In addition, Raman spectra of the sol–gel samples after reaction exhibit one extra peak at ≈1586 cm^{-1} (Fig. 11). After a long time on stream (stability studies) another extra band is observed at ≈1415 cm^{-1}. As an example, Fig. 11 shows also the Raman spectra obtained for the sol–gel sample calcined at 900 °C after the stability test at 800 °C. These bands can be assigned to the existence of carbon (graphite) on the surface that increases drastically after a long time on stream [75,76], confirming the surface modifications revealed by SEM. In particular, the band at ≈1586 cm^{-1} has been attributed to the existence of considerable fraction of carbon at grain boundaries [77]. For the intermetallic sample such bands were practically inexistent, even after a long time on stream at high temperature.

Finally, the surface of the bimetallic oxides was also studied by XPS before and after reaction. The Ce 3d region presents a complex structure of doublets typical of Ce^{4+} in CeO_2 [78,79] (Fig. 12A). The Cu 2p region is composed by two doublets with spin–orbit separations of 19.9 ± 0.1 eV and a multiplet structure characteristic of Cu^{2+} species, like CuO or $Cu(OH)_2$. Cu $2p_{3/2}$ components, centered at 933.8 ± 0.1 and 936.8 ± 0.5 eV, are assigned to Cu^{2+}

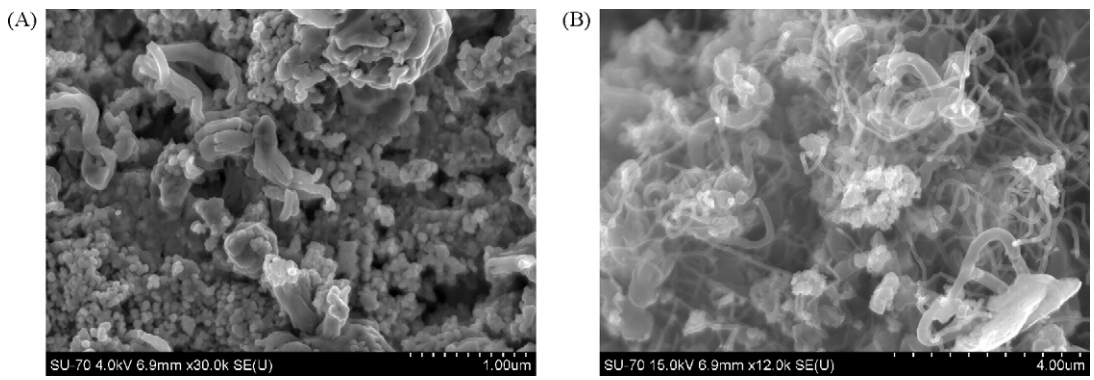

Fig. 8. SEM pictures obtained after reaction (A) and after a long time on stream (B) for the bimetallic copper–cerium oxide obtained by the sol–gel route after calcination at 250 °C.

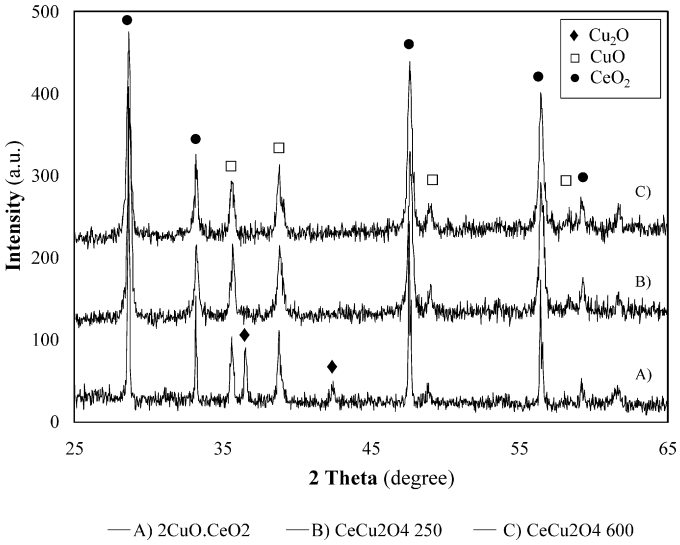

Fig. 9. XRD patterns obtained after reaction for the bimetallic copper–cerium oxides prepared by the intermetallic route (A) and by sol–gel (urea) after calcinations at 250 °C (B) and 600 °C (C).

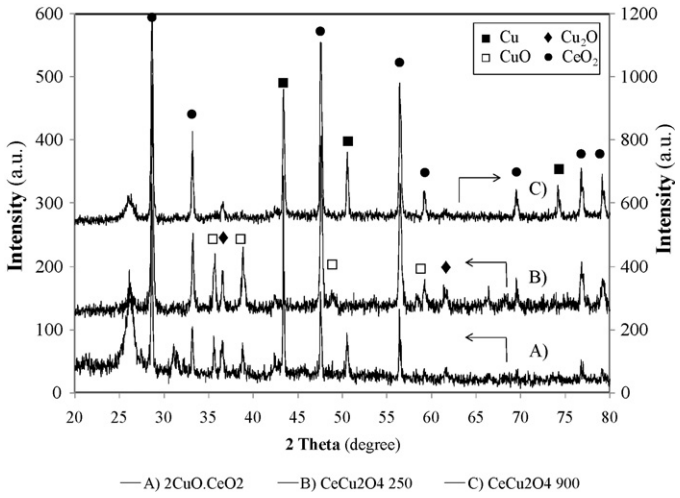

Fig. 10. XRD patterns obtained after the stability study for the bimetallic copper–cerium oxides prepared by the intermetallic route (A) and by sol–gel (urea) after calcinations at 250 °C (B) and 900 °C (C).

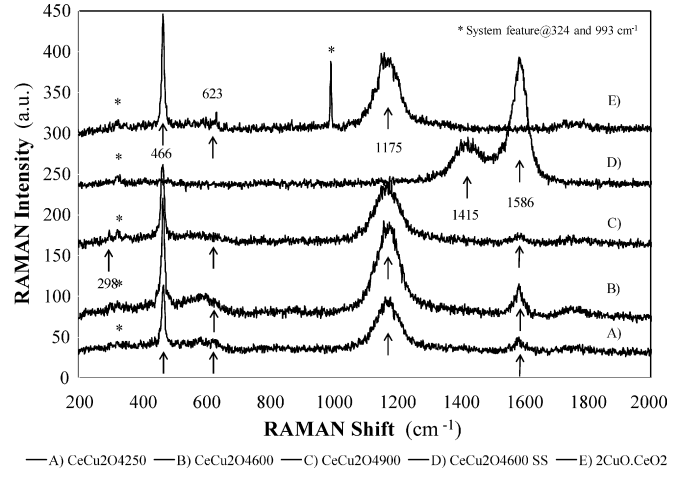

Fig. 11. UV-RAMAN spectra obtained after reaction and after the stability (SS) studies over the bimetallic copper–cerium oxide prepared by the sol–gel and intermetallic routes.

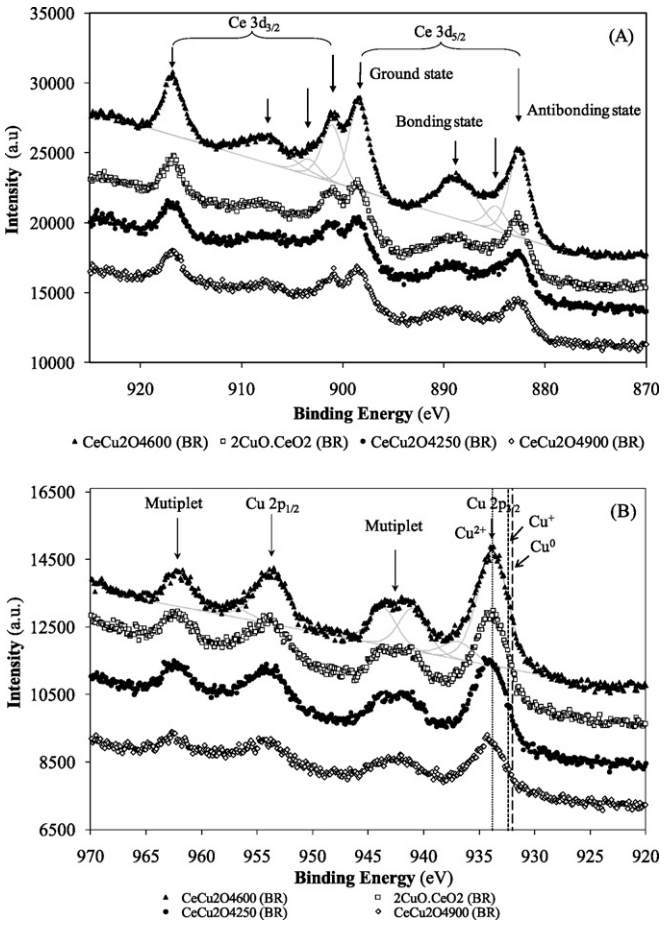

Fig. 12. XPS Ce 3d (A) and Cu 2p (B) regions for the intermetallic and sol–gel samples before reaction (BR).

bound to O and OH groups, respectively (Fig. 12B). However, the main peak centered at 933.8 eV is wide enough (3.3 ± 0.2 eV) to include also copper in other oxidation states, as shown by the dashed lines drawn in Fig. 12B, corresponding to Cu^{+} (Cu_2O) and Cu^{0}. However, Cu^{0} is unlikely to be detected on the extreme surface since it is expected to oxidize immediately after the sample is handled under the atmosphere. After reaction, no change in the binding energies (BE) of the Ce 3d and Cu 2p regions could be found.

C 1s is dominated by a peak centered at 285 eV corresponding to aliphatic carbon contamination, but in sol–gel samples and especially after reaction, it also includes an important contribution from graphite (~284.2 eV) that corroborates the results of Raman spectroscopy (Fig. 13). The main component of the O 1s region, centered at 529.8 ± 0.1 eV, is attributed to oxygen of metal or lanthanide oxides. At higher BE one can find two extra components centered at 531.8 ± 0.1 and 533.2 ± 0.2 eV, both presenting the contribution of oxygen in hydroxide and organic oxygen [80].

The quantitative XPS results show that the atomic Ce/Cu ratio is very similar in both synthetic methods. However, after reaction, there is a considerable enrichment in copper for the intermetallic samples, whereas for sol–gel samples the surface is depleted of copper, since the stoichiometric ratio should be Ce/Cu = 0.5 (Table 1).

Table 1 also presents the atomic oxygen/metal ratio. If the stoichiometric oxygen existed, this ratio should be:

$$\frac{0}{Ce + Cu} = \frac{2Ce/Cu + 1}{Ce/Cu + 1}$$

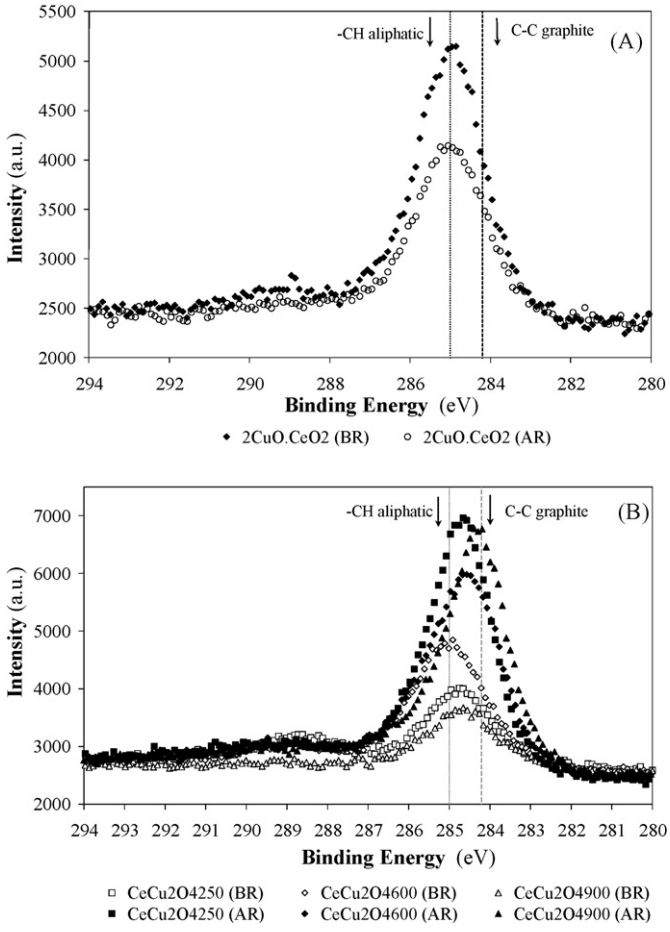

Fig. 13. XPS C 1s regions for regions for the intermetallic (A) and sol–gel samples (B) before (BR) and after reaction (AR).

Given the Ce/Cu ratio found for samples before reaction, the value should be around 1.4. This means that, in the all the samples, the oxygen exceeds the stoichiometric amount since the oxygen bound to carbon is almost negligible when compared to the total amount of oxygen. After reaction, the amount of oxygen in all the samples is similar within the experimental error. In fact, in the oxygen rich samples the relative amount of oxygen decreases a lot after reaction, whereas the sol–gel 250 and 600 samples slightly increase that amount.

Another interesting finding is that after reaction, the relative amount of carbon increases for the sol–gel samples while for the intermetallic ones it decreases (Fig. 13 and Table 1). This means that the reaction evolution seems to clean the surface of the intermetallic sample but poisons the surface of the sol–gel samples which correlates well with the Raman results. A possible explanation for this behavior is that the carbon seen by XPS in the intermetallic sample is completely external and then, easily removable by temperature increase and gas flow. Contrarily, in the other samples it is rather mixed with the other components and instead of being removed they can act as nucleation sites for further carbon compounds deposition poisoning the catalyst.

Therefore, the high activity and selectivity of the $2CuO{\cdot}CeO_2$ sample (intermetallic route) seem to be related to their stability to deactivation and to a major enrichment of the surface composition on copper and oxygen, as shown by the XPS results, which correlates with the surface morphologic differences found between the sol–gel and intermetallic route sample as shown by SEM/EDS. The lower activity and stability of the sol–gel samples seem to be the result of a smaller amount of copper species at the catalysts surface and deactivation due to carbon deposition that poisons their active sites [81]. Some copper particles may remain embedded in the ceria lattice and/or partially covered by carbon and could not be accessible to the reagents, which could also explain the slowdown of the increase of the activity for $T \geq 550\,^{\circ}C$ (Fig. 5).

A closer interaction between copper and ceria in the copper–ceria oxides and/or its higher dispersion certainly explains the higher copper reducibility on the sol–gel samples. It is clear that the CuO phase is reduced to metallic copper or at least partially to Cu_2O at the end of reaction. The XRD signals attributed to the Cu and Cu_2O phases were low, but very intense after a long time on stream (stability study). Furthermore, the catalysts were only active at temperatures higher than 350 °C, which could be correlated with the formation of Cu_2O and metallic copper, as expected from the H_2-TPR results, pointing out a major role of such species; it is known that a partially reduced metal clearly enhances the catalytic activity [82].

At last, the unusual H_2-TPR behavior of the intermetallic samples raises the possibility of an unusual interaction between copper and ceria species that could also contribute to their high activity and stability, particularly to a slowdown of the sintering of the copper particles at high reaction temperatures due to physical barriers established by the CeO_2 particles. As previously reported for nickel based catalysts, bulk diffusion of nickel atoms in lanthanum oxide perovskite-type structure is inhibited as a consequence of the physical barriers established by the La_2O_3 particles [83,84]. Moreover, the metallic Ni crystallites maintain a high dispersion on the La_2O_3 surface. On the basis of this argument, Fierro and coworkers [85] concluded that the good stability of the catalyst is mainly due to the ability to stabilize the Ni crystallites in a high dispersion degree on a La_2O_3 matrix, thus limiting the extent of the formation of aggregates of nickel particles. As a consequence, the formation of coke residues that would encapsulate or cover metallic Ni is also limited and hence the deactivation of the catalyst.

The same argument can be applied to the $2CuO{\cdot}CeO_2$ catalyst. Nevertheless, only the possibility of an unusual interaction between copper and ceria species on the intermetallic sample can explain the low reducibility of copper on that sample, which reinforces the importance of the close contact between CuO and CeO_2 that is a direct consequence of the synthetic method used in this work. However, this point deserves a deeper analysis in the near future.

4. Conclusions

The results obtained in the present work show that the copper–cerium oxide catalyst ($2CuO{\cdot}CeO_2$) obtained by the intermetallic route was very active and selective for the partial oxidation of methane and production of syngas suitable for the methanol and Fischer–Tropsch synthesis (Conv. $CH_4 > 90\%$, Sel. $H_2 > 99\%$, $H_2/CO \approx 2.0$) at $T = 750\,^{\circ}C$, which to our knowledge is a novelty on copper based catalysts. The catalytic performance of $2CuO{\cdot}CeO_2$ is only comparable to that of noble metals commercial catalysts, e.g. 5 wt% Rh/Al_2O_3. The influence of synthetic method on the catalytic performance was confirmed by comparison of such results with those of $CeCu_2O_4$ catalysts obtained by the sol–gel method in the presence of urea that were less active and selective than $2CuO{\cdot}CeO_2$. The copper–cerium oxide catalysts were quite stable in the temperature range studied, 350–800 °C, for a long period of time on stream and less expensive than the catalysts based on noble metals, which is an advantage of the intermetallic route. This work will be extended to other intermetallic compounds in order to find correlations along the lanthanide series and to study the influence of the *d* metal on their catalytic behavior.

Acknowledgment

This work was supported by the Portuguese "Fundação para a Ciência e a Tecnologia" under the contract PTDC/EQU-EQU/65126/2006.

Appendix A. Supplementary data

Supplementary data associated with this article can be found, in the online version, at doi:10.1016/j.molcata.2009.12.014.

References

[1] C. Mateos-Pedrero, C. Cellier, P. Eloy, P. Ruiz, Catal. Today 128 (2007) 216–222.
[2] E.P.J. Mallens, J.H.B.J. Hoebink, G.B. Marin, J. Catal. 167 (1997) 43–56.
[3] M. Fathi, K.H. Hofstad, T. Sperle, O.A. Rokstad, A. Holmen, Catal. Today 42 (1998) 205–209.
[4] K. Sekizawa, H. Widjaja, S. Maeda, Y. Ozawa, K. Eguchi, Catal. Today 59 (2000) 69–74.
[5] S. Rabe, M. Nachtegaal, F. Vogel, Phys. Chem. Chem. Phys. 9 (2007) 1461–1468.
[6] A. Donazzi, A. Beretta, G. Groppi, P. Forzatti, J. Catal. 255 (2008) 241–258.
[7] A. Slagtern, H.M. Swaan, U. Olsbye, I.M. Dahl, C. Mirodatos, Catal. Today 46 (1998) 107–115.
[8] R.C. Jin, Y.X. Chen, W.Z. Li, W. Cui, Y.Y. Ji, C.Y. Yu, Y. Jiang, Appl. Catal. A 201 (2000) 71–80.
[9] J. Barbero, M.A. Pena, J.M. Campos-Martin, J.L.G. Fierro, P.L. Arias, Catal. Lett. 87 (2003) 211–218.
[10] V.R. Choudhary, V.H. Rane, A.M. Rajput, Appl. Catal. A 162 (1997) 235–238.
[11] J.M. Li, F.Y. Huang, W.Z. Weng, X.Q. Pei, C.R. Luo, H.Q. Lin, C.J. Huang, H.L. Wan, Catal. Today 131 (2008) 179–187.
[12] H.Y. Wang, C.T. Au, Appl. Catal. A 155 (1997) 239–252.
[13] M.C.J. Bradford, M.A. Vannice, J. Catal. 183 (1999) 69–75.
[14] J.R. Rostrupnielsen, J.H.B. Hansen, J. Catal. 144 (1993) 38–49.
[15] R. Lago, G. Bini, M.A. Pena, J.L.G. Fierro, J. Catal. 167 (1997) 198–209.
[16] V.R. Choudhary, B.S. Uphade, A.A. Belhekar, J. Catal. 163 (1996) 312–318.
[17] V.A. Tsipouriari, X.E. Verykios, J. Catal. 179 (1998) 292–299.
[18] N.V. Skorodumova, S.I. Simak, B.I. Lundqvist, I.A. Abrikosov, B. Johansson, Phys. Rev. Lett. 89 (2002).
[19] A.E.C. Palmqvist, E.M. Johansson, S.G. Jaras, M. Muhammed, Catal. Lett. 56 (1998) 69–75.
[20] E. Ramirez-Cabrera, A. Atkinson, D. Chadwick, Appl. Catal. B-Environ. 36 (2002) 193–206.
[21] K. Otsuka, T. Ushiyama, I. Yamanaka, Chem. Lett. (1993) 1517–1520.
[22] K. Otsuka, E. Sunada, T. Ushiyama, I. Yamanaka, Nat. Gas Convers. IV 107 (1997) 531–536.
[23] K. Otsuka, Y. Wang, E. Sunada, I. Yamanaka, J. Catal. 175 (1998) 152–160.
[24] Q. Miao, G.X. Xiong, S.S. Sheng, W. Cui, L. Xu, X.X. Guo, Appl. Catal. A 154 (1997) 17–27.
[25] L. Cao, Y. Chen, W. Li, Nat. Gas Convers. IV 107 (1997) 467–471.
[26] S.M. Stagg, D.E. Resasco, Nat. Gas Convers. V 119 (1998) 813–818.
[27] S. Tang, J. Lin, K.L. Tan, Catal. Lett. 51 (1998) 169–175.
[28] M.F. Luo, Y.J. Zhong, X.X. Yuan, X.M. Zheng, Appl. Catal. A 162 (1997) 121–131.
[29] W. Liu, M. Flytzani-Stephanopoulos, J. Catal. 153 (1995) 304–316.
[30] B. Skarman, D. Grandjean, R.E. Benfield, A. Hinz, A. Andersson, L.R. Wallenberg, J. Catal. 211 (2002) 119–133.
[31] G. Avgouropoulos, T. Ioannides, Appl. Catal. A 244 (2003) 155–167.
[32] W. Liu, M. Flytzani-Stephanopoulos, J. Catal. 153 (1995) 317–332.
[33] W. Liu, M. Flytzani-Stephanopoulos, Chem. Eng. J. 64 (1996) 283.
[34] C. Hardacre, R.M. Ormerod, R.M. Lambert, J. Phys. Chem. 98 (1994) 10901–10905.
[35] L. Kundakovic, M. Flytzani-Stephanopoulos, J. Catal. 179 (1998) 203–221.
[36] F. Zamar, A. Trovarelli, C. Deleitenburg, G. Dolcetti, J. Chem. Soc.-Chem. Commun. (1995) 965–966.
[37] P. Braos-Garcia, P. Maireles-Torres, E. Rodriguez-Castellon, A. Jimenez-Lopez, J. Mol. Catal. A 193 (2003) 185–196.
[38] L.L. Hench, J.K. West, Chem. Rev. 90 (1990) 33–72.
[39] J.S. Abell, Preparation and crystal growth of rare earth elements and intermetallic compounds, in: A. Karl, Gschneidner Jr., LeRoy Eyring (Eds.), Handbook on the Physics and Chemistry of Rare Earth, North-Holland Publishing Company, Amsterdam, 1989, pp. 1–51.
[40] D. Ballivet-Tkatchenko, J. Branco, A.P. de Matos, J. Phys. Chem. 99 (1995) 5481–5484.
[41] J.B. Branco, D. Ballivet-Tkatchenko, A. Pires de Matos, J. Mol. Catal. A, Chemical 307 (2009) 37–42.
[42] J. Branco, C. de Jesus Dias, A.P. Goncalves, T.A. Gasche, A.P. de Matos, Thermochim. Acta 420 (2004) 169–173.
[43] J.B. Branco, T.A. Gasche, A.P. Goncalves, A.P. de Matos, J. Alloys Compd. 323 (2001) 610–613.
[44] K.H.J. Buschow, Hydrogen absorption in intermetallic compounds, in: A. Karl, Gschneidner Jr., LeRoy Eyring (Eds.), Handbook on Physics and Chemistry of Rare Earth, North-Holland Publishing Company, Amsterdam, 1984, pp. 1–111.
[45] A. Iandelli, A. Palenzona, Crystal chemistry of intermetallic compounds, in: A. Karl, Gschneidner Jr., LeRoy Eyring (Eds.), Handbook on the Physics and Chemistry of Rare Earth, North-Holland Publishing Company, Amsterdam, New York, Oxford, 1979, pp. 1–54.
[46] G. Sandrock, S. Suda, L. Sclapbach, in: L. Sclapbach (Ed.), Topics in Applied Physics, Springer-Verlag, Berlin, Heidelberg, New York, 1992, pp. 197–258.
[47] W.E. Wallace, J. France, A. Shamsi, in: G.J. MaCarthy, J.J. Rhyne, H.S. Silber (Eds.), Catalysis using Rare Earth and Actinide Intermetallics, Plenum Press, New York, London, 1982, p. 561.
[48] G.B. Atkinson, E.G. Baglin, L.J. Nicks, D.J. Bauer, in: R.G. Herman (Ed.), Catalytic Conversions of Synthesis Gas and Alcohols to Chemicals, Plenum Press, New York, London, 1984, p. 65.
[49] E.G. Baglin, G.B. Atkinson, L.J. Nicks, Ind. Eng. Chem., Prod. Res. Dev. 20 (1981) 87–90.
[50] V.T. Coon, T. Takeshita, W.E. Wallace, R.S. Craig, J. Phys. Chem. 80 (1976) 1878–1879.
[51] J.B. Branco, D. Ballivet-Tkatchenko, A.P. de Matos, J. Phys. Chem. C 111 (2007) 15084–15088.
[52] J. Mahia, J.L. Martinez Lorenzo, M.C. Blanco, M.A. Lopez Quintela, J. Solid State Chem. 131 (1997) 246–251.
[53] JCPDS, The Powder Diffraction File, JCPDS, 1601 Park Avenue, Swarthmore, PA, 1981.
[54] V. Uvarov, I. Popov, Mater. Charact. 58 (2007) 883–891.
[55] A. Garbout, S. Bouattour, A.M.B. do Rego, A. Ferraria, A.W. Kolsi, J. Cryst. Growth 304 (2007) 374–382.
[56] D. Ballivet-Tkatchenko, G. Delahay, J. Therm. Anal. 41 (1994) 1141.
[57] D. Ballivet-Tkatchenko, G. Delahay, J. Therm. Anal. 41 (1994) 1141–1151.
[58] D.A. Hickman, L.D. Schmidt, Science 259 (1993) 343–346.
[59] A. Badri, J. Lamotte, J.C. Lavalley, A. Laachir, V. Perrichon, O. Touret, G.N. Sauvion, E. Quemere, Eur. J. Solid State Inorg. Chem. 28 (1991) 445–448.
[60] W.J. Shan, Z.C. Feng, Z.L. Li, Z. Jing, W.J. Shen, L. Can, J. Catal. 228 (2004) 206–217.
[61] A. Martinez-Arias, D. Gamarra, M. Fernandez-Garcia, X.Q. Wang, J.C. Hanson, J.A. Rodriguez, J. Catal. 240 (2006) 1–7.
[62] R. Inguanta, S. Piazza, C. Sunseri, Nanotechnology 18 (2007).
[63] M.S.P. Francisco, V.R. Mastelaro, P.A.P. Nascente, A.O. Florentino, J. Phys. Chem. B 105 (2001) 10515–10522.
[64] A. Martinez-Arias, A.B. Hungria, M. Fernandez-Garcia, J.C. Conesa, G. Munuera, J. Phys. Chem. B 108 (2004) 17983–17991.
[65] S.H. Zeng, X. Bai, X.Y. Wang, W.G. Yu, Y. Liu, J. Rare Earths 24 (2006) 177–181.
[66] D.D. Wagman, W.H. Evans, V.B. Parker, R.H. Schumm, I. Halow, S.M. Bailey, K.L. Churney, R.L. Nuttall, J. Phys. Chem. Ref. Data 11 (Suppl. 2) (1982).
[67] C. de Leitenburg, A. Trovarelli, J. Kaspar, J. Catal. 166 (1997) 98–107.
[68] J.B. Branco, D. Ballivet-Tkatchenko, A.P. de Matos, J. Alloys Compd. 464 (2008) 399–406.
[69] G. Wrobel, C. Lamonier, A. Bennani, A. DHuysser, A. Aboukais, J. Chem. Soc.-Faraday Trans. 92 (1996) 2001–2009.
[70] P. Ratnasamy, D. Srinivas, C.V.V. Satyanarayana, P. Manikandan, R.S.S. Kumaran, M. Sachin, V.N. Shetti, J. Catal. 221 (2004) 455–465.
[71] M. He, M.F. Luo, P. Fang, J. Rare Earths 24 (2006) 188–192.
[72] J.A. Rodriguez, M. Perez, J. Evans, G. Liu, J. Hrbek, J. Chem. Phys. 122 (2005) 241101.
[73] J.A. Rodriguez, X. Wang, P. Liu, W. Wen, J.C. Hanson, J. Hrbek, M. Perez, J. Evans, Top. Catal. 44 (2007) 73–81.
[74] X.Y. Zhao, J. Hrbek, J.A. Rodriguez, M. Perez, Surf. Sci. 600 (2006) 229–239.
[75] F.J. Garcia-Rodriguez, J. Gonzalez-Hernandez, F. Perez-Robles, Y.V. Vorobiev, A. Manzano-Ramirez, S. Jimenez-Sandoval, B.S. Chao, J. Raman Spectrosc. 29 (1998) 763–771.
[76] A. Das, B. Chakraborty, A.K. Sood, Bull. Mater. Sci. 31 (2008) 579–584.
[77] H. Torii, Chem. Phys. Lett. 414 (2005) 417–422.
[78] P. Burroughs, A. Hamnett, A.F. Orchard, G. Thornton, J. Chem. Soc.-Dalton Trans. (1976) 1686–1698.
[79] A. Kotani, H. Ogasawara, J. Electron Spectrosc. Relat. Phenom. 60 (1992) 257–299.
[80] G. Beamson, D. Briggs, High Resolution XPS of Organic Polymers. The Scienta ESCA300 Database, John Wiley & Sons, New York, 1992.
[81] C.H. Kim, L.T. Thompson, J. Catal. 230 (2005) 66–74.
[82] X.Q. Wang, J.A. Rodriguez, J.C. Hanson, D. Gamarra, A. Martinez-Arias, M. Fernandez-Garcia, J. Phys. Chem. B 110 (2006) 428–434.
[83] G.H. Li, L.J. Hu, J.M. Hill, Appl. Catal. A 301 (2006) 16–24.
[84] J.I. Villacampa, C. Royo, E. Romeo, J.A. Montoya, P. Del Angel, A. Monzon, Appl. Catal. A 252 (2003) 363–383.
[85] M.E. Rivas, J.L.G. Fierro, R. Guil-Lopez, M.A. Pena, V. La Parola, M.R. Goldwasser, Catal. Today 133 (2008) 367–373.